New Journal of Physics
The open–access journal for physics

Symmetry breaking in few layer graphene films

Aaron Bostwick[1], Taisuke Ohta[1,2], Jessica L McChesney[1,3], Konstantin V Emtsev[4], Thomas Seyller[4], Karsten Horn[2] and Eli Rotenberg[1,5]

[1] Advanced Light Source, E O Lawrence Berkeley National Laboratory, Berkeley, CA 94720, USA
[2] Department of Molecular Physics, Fritz-Haber-Institut der Max-Planck-Gesellschaft, Faradayweg 4-6, 14195 Berlin, Germany
[3] Department of Physics, Montana State University, P O Box 173840, Bozeman, MT 59717-3840, USA
[4] Institut für Physik der Kondensierten Materie, Lehrstuhl für Technische Physik, Universität Erlangen-Nürnberg, Erwin-Rommel-Straße 1, D-91058 Erlangen, Germany
E-mail: erotenberg@lbl.gov

New Journal of Physics **9** (2007) 385
Received 22 May 2007
Published 31 October 2007
Online at http://www.njp.org/
doi:10.1088/1367-2630/9/10/385

Abstract. Recently, it was demonstrated that the quasiparticle dynamics, the layer-dependent charge and potential, and the *c*-axis screening coefficient could be extracted from measurements of the spectral function of few layer graphene films grown epitaxially on SiC using angle-resolved photoemission spectroscopy (ARPES). In this paper we review these findings, and present detailed methodology for extracting such parameters from ARPES. We also present detailed arguments against the possibility of an energy gap at the Dirac crossing E_D.

[5] Author to whom any correspondence should be addressed.

PII: S1367-2630(07)50983-3

Contents

1. Introduction

1.1. Isolation of graphene

Recently, much attention has been given to the electronic and other properties of graphene. Following the isolation and dramatic transport measurements of individual graphene flakes by exfoliation [1]–[3], there has been an explosion of theoretical and experimental interest in graphene. Among the interesting properties found are the massless, relativistic nature of graphene's carriers, and the impact of Berry's topological phase factor on the transport properties of single and bilayer graphene. Especially interesting from a technological point of view is the extremely long lifetime of carriers [4], whose origin is currently under debate (see for example [5] and references therein). Among the possible contributions to this long carrier lifetime is a weak backscattering arising from their chiral nature, which in nanotubes leads to a lack of backscattering [6, 7]. This chiral nature derives from special symmetry properties of the graphene lattice.

Exploitation of these effects for electronic devices requires the precise and scalable control of graphene nanostructures, which cannot as yet be achieved with exfoliated flakes. Therefore, much attention has been given to the epitaxial growth of graphene on various substrates. Forbeaux *et al* [8] were the first to demonstrate that high-quality epitaxy of single and few-layer graphene (FLG) could be achieved on the silicon-rich SiC(0001) surface. Transport measurements and demonstration of the feasibility of patterned graphene devices were demonstrated by Berger *et al* [4, 9].

Figure 1 shows the atomic arrangement in monolayer and bilayer of graphene. The unit cell consists of two equivalent C atoms, labelled A and B with bond length 1.42 Å. Jones proved that for a closed-packed hexagonal lattice, the energy gap along the zone boundary disappears where bands from adjacent unit cells cross [10]. This is illustrated in figure 2, which shows the tight-binding (TB) band structure $E(\mathbf{k})$ of graphene, evaluated to third nearest neighbour using the parameters of Reich [11]. (Here we restrict consideration to the π and the π^* states, which are derived from the p_z orbitals of the carbon atoms [12].) Quantitative fits of the TB model to experimentally determined bands were presented by Bostwick *et al* [13]. These states meet at the so-called Dirac crossing point at energy E_D in agreement with Jones' theorem. For neutral (undoped) graphene, the Fermi energy (the energy of the least-bounds states) $E_F = E_D$.

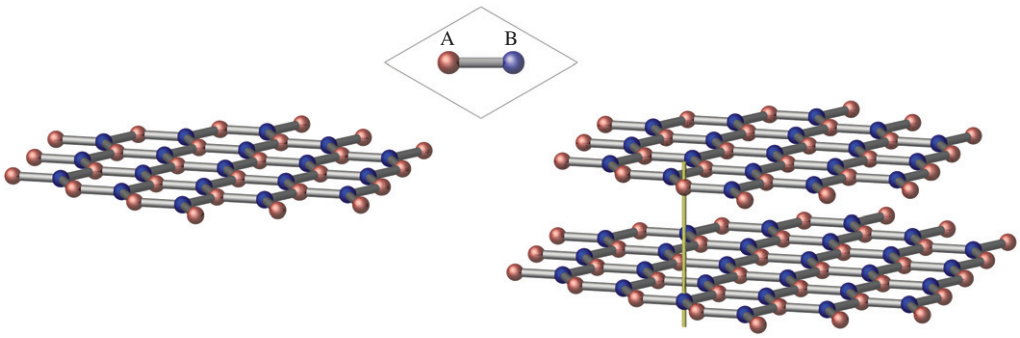

Figure 1. Atomic arrangement in (left) monolayer and (right) bilayer graphene. The inset shows the unit cell with two equivalent atoms.

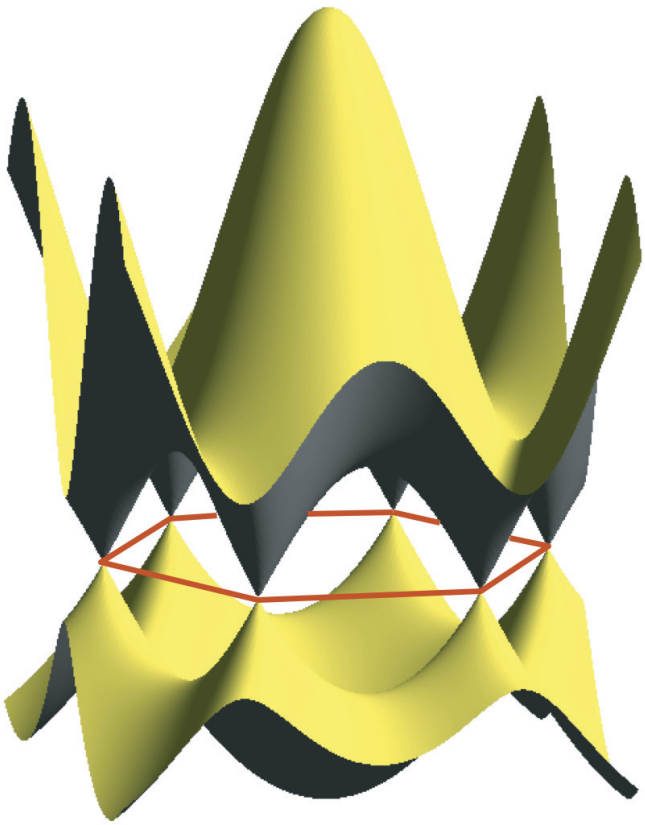

Figure 2. Theoretical TB band structure for graphene, based on third NN parameters due to Reich *et al* [11].

Many of the interesting properties of graphene revolve around the fact that the band crossing at E_D is strictly gapless. This means that at zero doping and zero temperature, graphene is a gapless semiconductor or a zero-overlap semimetal. On doping the graphene by either deposition of foreign atoms [14, 15], molecules [16] or in a gated geometry [1]–[3], the carrier density can be easily manipulated. With this control, we can systematically study the many-body interactions in graphene as a function of doping using angle-resolved photoemission spectroscopy (ARPES).

1.2. ARPES

The Fermi surface is defined as a constant energy surface $E(\mathbf{k})|_{E=E_F}$, and determines all the transport properties of conducting materials. While transport measurements on doped graphene can determine the relevant properties such as group velocity and lifetime of carriers on the Fermi surface, ARPES is a useful complementary tool. It can determine the electronic band structure, so it is capable of measuring not only the group velocity and Fermi surface, but also the constant-energy surfaces for all occupied states and the full occupied bandstructure $E(\mathbf{k})$. Furthermore, the technique also accesses important information about many-body effects [17]. When there is sufficient energy and momentum resolution, the experimentally determined momentum width of the Fermi contours can be taken to be the inverse of the mean free path, and the measurement of $E(\mathbf{k})$ is taken as a measure of the many-body spectral function $A(\mathbf{k}, \omega)$.

This spectral function is in turn related to an electronic self-energy $\Sigma(\mathbf{k}, \omega)$ as follows (see [18] and therein):

$$A(\mathbf{k}, \omega) = \frac{|\mathrm{Im}\ \Sigma(\mathbf{k}, \omega)|}{(\omega - \omega_b(\mathbf{k}) - \mathrm{Re}\ \Sigma(\mathbf{k}, \omega))^2 + (\mathrm{Im}\ \Sigma(\mathbf{k}, \omega))^2}, \tag{1}$$

where ω is the measured binding energy and $\omega_b(\mathbf{k})$ is another energy defined below (where $\hbar = 1$). We make the approximation that $\Sigma(\mathbf{k}, \omega)$ is $\mathbf{k}$-independent. In this form, we see that $A(\mathbf{k}, \omega)$, when evaluated at constant energy ω, is a Lorentzian function whose width is given by $\mathrm{Im}\Sigma$ representing the inverse lifetime (proportional to the inverse mean free path).

Equation (1) is valid when the scattering rate of the charge carriers (expressed in energy units) is not too large compared to their energy. In this situation, we refer to the charge carriers as quasiparticles (QPs). In our measurements, the QPs are holes which have been injected as part of the photoemission process. Their binding energy ω (here $\hbar = 1$) is taken as a negative number, and we speak of increasing energy as an increase in this negative value.

One can draw an analogy between QPs propagating in a scattering medium and light travelling in a lossy optical medium. Such a medium is characterized by a complex dielectric function, and the effects on the light propagation are not only through its absorption but also a dispersion. To satisfy causality, the real and imaginary parts of the dielectric function are related by a Hilbert transformation. Similarly, the propagation of QPs in a scattering medium leads not only to inelastic scattering (whose lifetime is encoded in Im Σ) but also to renormalization of the carrier's energy, encoded in the real part of $\Sigma(\mathbf{k}, \omega)$. These real and imaginary parts of $\Sigma(\mathbf{k}, \omega)$ are also related by a Hilbert transform, and the function Re Σ is defined as the difference between the measured carrier energy ω and the 'bare' band energy $\omega_b(\mathbf{k})$ (that is, in the absence of scattering interactions), as indicated in equation (1). Following this formalism, ARPES can determine the energy-dependent lifetime due to scattering from other excitations in the system.

For a valid spectral function analysis, the ARPES spectra must be acquired with sufficient resolution and the samples must be of high quality so that defect scattering is negligible. They must also be well-characterized in thickness to ensure that the pure graphene signal is accessed.

The first ARPES measurements on FLG on SiC were from thick films [19]–[21] aimed toward studying the properties of graphite. Later, Rollings *et al* [22] measured the Fermi surface and other constant energy surfaces around E_D for a film with thicknesses around 2–3 layers, determined by core level shifts of C 1s electrons. Systematic core level and valence band offset studies were carried out around the same time by Seyller *et al* [23]. Because of the contribution of

carbon from the SiC substrate to the core level signal, such measurements give a rough measure of the film thickness but cannot give a precise thickness measurement.

As shown below, the ARPES measurements themselves can give not only a precise thickness determination, but also determine other crucial quantities. The initial formation of the graphene valence band from the silicon-rich SiC surface through to the first monolayer of graphene was by Emtsev *et al* [24]. Valence band measurements to discriminate film thicknesses greater than 1 monolayer were first shown by Ohta *et al* [14] for bilayer and later systematically for monolayer–quadlayer graphene films [25].

These studies also demonstrated the crucial role of substrate preparation for good quality valence band measurements. The first detailed spectral function by ARPES from graphene were published by Bostwick *et al* [15] and could show a rich spectrum dominated by electron–electron, electron–phonon (e–ph), and electron–plasmon (e–pl) scattering.

2. Experimental

Here, we briefly review the growth method of graphene on SiC in our work [14, 15, 25]. Films were grown on *n*-type ($\sim 10^{18}\,\mathrm{cm}^{-3}$ N atoms) SiC(0001) wafers which were precleaned by annealing in 1 bar of hydrogen gas at 1550°C for around 30 min. The role of this cleaning step is essential, as by etching it removes the polishing scratches while maintaining bulk SiC stoichiometry. As-cleaned substrates were found to be atomically flat with wide terraces (Ohta *et al* unpublished). Formation of graphene layers by heating to around 1200°C in ultrahigh vacuum was monitored with low-energy electron diffraction (LEED) following Forbeaux *et al* [8] and ARPES as described below. The base pressure of our system was $1\text{–}2 \times 10^{-11}$ T, and graphene growth was always performed at pressures better than 1×10^{-10} T. All measurements were obtained at phonon energy $h\nu = 94$ eV unless otherwise noted.

3. Symmetry breaking considerations for FLG

3.1. Monolayer graphene: a gap at E_D due to symmetry breaking?

As Forbeaux *et al* [8] showed, FLG formation is accompanied by a $6\sqrt{3} \times 6\sqrt{3}$ reconstruction at the graphite–SiC interface, which was initially attributed to the interference between the graphene and SiC lattice constants. We now know from photoemission [24], theoretical calculations [26, 27], and scanning tunnelling microscopy (STM) [28] that the $6\sqrt{3} \times 6\sqrt{3}$ represents a non-interacting '0th' graphene layer whose electronic structure resembles graphene only insofar as it has intact σ-like bands (derived from sp^2-hybridized in-plane bonds) but is lacking the π bands characteristic of the out-of-plane p_z states of graphene. The presence of such a 0th layer is important because it acts like a dead layer, saturating or interacting with the underlying SiC bonds while forming a template for a subsequent first graphene overlayer. From symmetry considerations, it is known that the π bands from the latter and the σ bands of the former cannot interact. Therefore, the first graphene layer's chemical interaction with the substrate is very weak, and we expect the π bands of graphene on SiC are to a very good approximation the same as those of freestanding-doped graphene. In the following, we do not count this dead 0th layer among the active graphene layers in our FLG film.

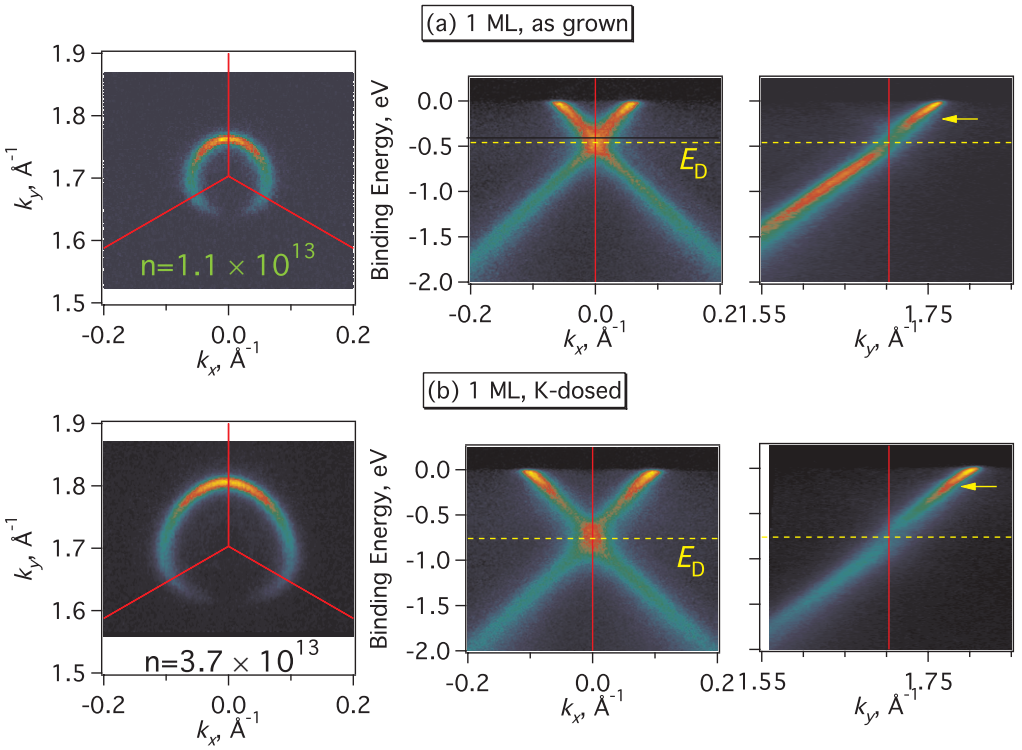

Figure 3. Experimental Fermi surfaces (left panels) and band structures (middle and, right panels) for (a) as-prepared monolayer graphene and (b) graphene dosed with K atoms. The middle and right panels are taken along orthogonal directions through the K point as indicated. Adapted from [15]. The doping levels in electrons per cm^2 are indicated. The phonon kinks at ~ 200 meV are indicated by arrows.

It is well-known that the Hamiltonian of one layer of graphene near the K point of the Brillouin zone can be approximated [6, 7, 29, 30] by

$$\mathcal{H} = \begin{pmatrix} E_1 + \Delta/2 & v(k_x - \mathrm{i}k_y) \\ v(k_x + \mathrm{i}k_y) & E_1 - \Delta/2 \end{pmatrix} \equiv \begin{pmatrix} E_1 + \Delta/2 & v\pi^\dagger \\ v\pi & E_1 - \Delta/2 \end{pmatrix} \equiv \alpha_1, \tag{2}$$

where the wavefunctions $\Psi = (\psi_A, \psi_B)$ are written in terms of p_z orbitals centred on the A and B atoms in the graphene basis set. The parameter Δ represents a possible asymmetry between the A and B sites. For ordinary graphene, $\Delta = 0$ since the atoms are indistinguishable. The off-diagonal terms represent the hopping between A and B sublattices, and v is the band velocity around E_D.

The Hamiltonian in equation (2) leads to a conical bandstructure $E(\mathbf{k}) = vk$ when $\Delta = 0$. Here $\mathbf{k}$ is the momentum relative to one of the K points at the corner of the graphene Brillouin zone (see figure 2). Experimental Fermi surfaces and underlying bandstructures for clean and alkali-dosed graphene are shown in figures 3(a) and (b), adapted from [15]. We can immediately recognize the expected nearly linear dispersions as well as the Dirac crossing points (middle panels) in the bands at the Dirac energy E_D. We also see that there is a nontrivial change in intensity when traversing around the Fermi contour. This will be discussed in detail below, but for now we regard it as a photoemission cross-section effect. Because of this effect, when we

sample the bandstructure in the y-direction (relative to figure 3), we see only one of the two expected bands; the other is extinguished (right panels).

We also observe that even the clean, as-grown graphene films have a Fermi level E_F significantly above (by around 0.45 eV) the Dirac energy E_D. This in-built doping was first reported by Rollings *et al* [22] and can be attributed to the greater electron affinity of graphene compared to the substrate. Our experiments have shown that this intrinsic n-doping is independent of whether the substrate dopants have been frozen out (at $T \sim 40$ K). Since its discovery by ARPES, this intrinsic n-doping has also been predicted theoretically [26, 27].

An important feature of the one monolayer data is the appearance of kinks in the energy band structure below E_F [15]. These kinks occur at two energy scales. First, we see a slight kink at $\sim$200 meV below E_F. This kink is hardly visible on the large energy scale plotted in figure 3, but it is accompanied by pronounced sharpening between 200 meV and E_F that is readily observed. This kink is similar to the ones which have been observed at similar energy scale in graphite [31, 32] and bilayer graphene [14] that have been attributed to e–ph scattering. We can understand the presence of the kink within the spectral function formalism in equation (1), noting that there is an observable increase in linewidth of the band at binding energies greater than 200 meV, signifying a decrease in the lifetime of the states as electrons absorb or emit phonons. We will discuss this formalism further below but for now it is sufficient to identify this feature with phonons for two reasons: firstly because of the energy scale, which corresponds to the in-plane LO and TO phonons, and secondly, because the kink feature's energy scale remains constant with doping, as expected for the small doping levels considered here.

There is a second anomaly in the dispersion around the Dirac crossing point in figure 3. In the middle panels, where both bands have equal intensity, the region of the crossing of the bands seems spread out in energy. In the right panels, where one band is extinguished, it appears that this spread is associated with a second kink feature which is at the Dirac crossing point of the bands. Unlike the phonon kink, this anomaly moves to higher binding energy with doping, and must therefore be somehow associated with the Dirac energy E_D. Similar to the phonon kink, it is stronger at higher doping, and it is associated with a change in linewidth—the bands are locally broadened around E_D.

What causes this second feature? In Bostwick *et al* [15], it was proposed to be a kink due to e–pl interaction but it has been recently proposed that the observed spreading of the bands around E_D is associated with substrate-dependent energy gap at E_D [33, 34]. Such a gap would be interesting because it suggests an electronic or chemical control of the electronic character (two-dimensional (2D) semimetal versus semiconductor) and is proposed on the basis of possible symmetry breaking. First, we discuss this idea and then present the evidence against it followed by evidence in favour of the e–pl scattering model.

Within the simple Hamiltonian (equation (2)) a gap of magnitude Δ appears at the Dirac crossing energy E_D when the parameter $\Delta \neq 0$. A physical interpretation of this gap is the symmetry breaking of the A and B atoms. This occurs for, e.g. replacement of C atoms with B and N in hexagonal boron nitride. It also occurs in a scenario where the bonding of A and B atoms to the 0th layer is asymmetric as recently proposed [33, 34].

We present arguments against this scenario in graphene on SiC as follows.

1. The interaction between the 1st and 0th layer is very weak. This was established by ARPES [24], theory [26, 27], and STM [28]. A possible argument against the weak interlayer attraction is the appearance in monolayer graphene films of replica π bands with $6\sqrt{3} \times 6\sqrt{3}$

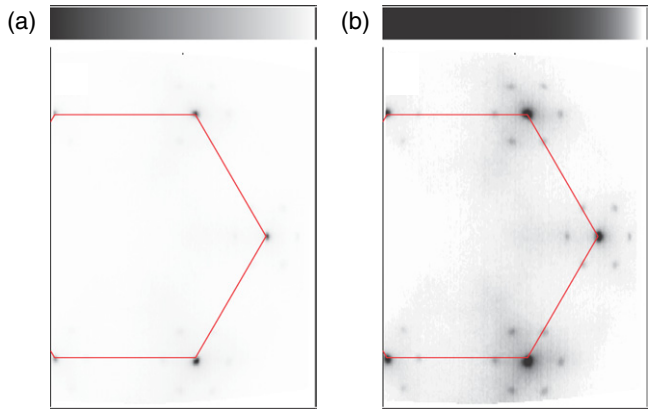

Figure 4. Constant energy surface at the Dirac energy E_D for (a) ordinary linear intensity scale and (b) highly nonlinear intensity scale. The weak satellite bands barely visible with a linear scale are highlighted at the right. The remaining background intensity is attributed to the $6\sqrt{3} \times 6\sqrt{3}$ interface layer. The sample is as-grown graphene, and measurements were at $T \sim 25$ K.

symmetry, ascribed by us as due to diffraction of the outgoing photoelectrons [15], similar to other nearly incommensurate systems [35]. These satellite bands lead to replicas of the constant energy contours, illustrated for the Dirac crossing energy in figure 4. With a linear grey scale in (a) the replica bands are hardly noticeable but with a highly non-linear grey scale figure 4(b), they can be emphasized.

It is tempting to ascribe the replica bands to a possible $6\sqrt{3} \times 6\sqrt{3}$ superlattice potential felt by the first graphene layer. If this were true, additional energy minigaps would appear where the replica and main bands cross [36]; however, no such gaps have been observed [14]. Furthermore, the replica bands, very weak at low temperature (about a factor 40 reduced intensity compared to the primary band) do not appear at room temperature [24] and at 100 K are dramatically broadened (J L McChesney, unpublished). This observation violates the hypothesis that the first graphene layer has $6\sqrt{3} \times 6\sqrt{3}$ symmetry potential which would demand the linewidths of the replica and main bands to be identical by symmetry. Instead, we can easily understand the broadening of the replica bands as due to a Debye–Waller factor, confirming the origin of these replica bands as due to final-state diffraction.

2. The doping dependence shows a clear increase in the spread of the states at the Dirac crossing. If this spread were due to a gap from coupling to the substrate, the coupling strength should be independent of the doping density (or become smaller due to enhanced screening).
3. We observed that the bands above and below E_D are misaligned [15], so that the projections of the π states below E_D do not pass through the π^* states above E_D. This is illustrated by the dashed lines in figure 5(a), which reproduces the clean graphene bandstructure. This misalignment does not occur in the energy gap scenario, but comes naturally when many-body interactions are present.
4. DOS does not show a gap at E_D. This is illustrated in figure 5(b) for the momentum-integrated DOS. In a gap scenario, one expects a decreased DOS but we see a peak (expected for crossed bands).

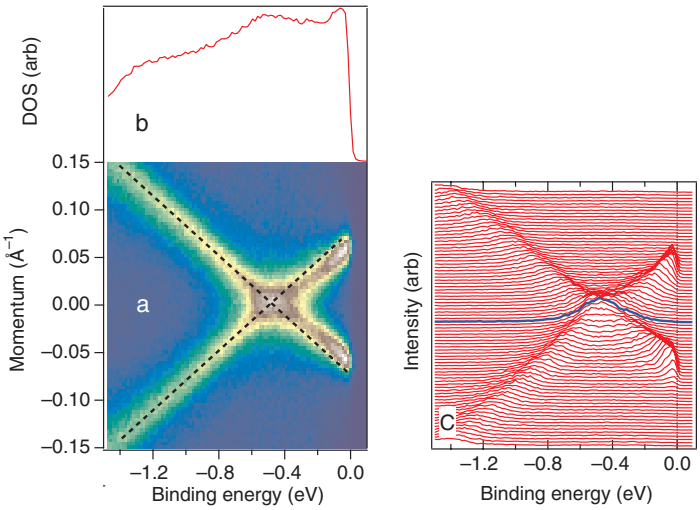

Figure 5. (a) Bandstructure for as-prepared graphene. The dashed lines are a projection of the π bands and highlight the fact that this projection does not pass through the π^* bands above E_D. (b) The momentum-integrated density of states, derived by integrated the bandstructure in (a). No dip in the density of states (DOS) is observed at the Dirac crossing point. (c) The individual energy distribution curves (EDCs) for the bands in (a). The centre EDC that includes the Dirac crossing shows no resolved splitting, which would be expected for a gap.

5. The EDC at the Dirac crossing shows only a single peak, not a split peak as expected in a gap scenario (see figure 5(c)).
6. The intensity distribution along the Fermi surface provides a stringent test for A–B atom symmetry breaking. It is observed that one side of the Fermi contours is very weak or absent. In the strictly symmetric case $\Delta = 0$, the intensity on one side of the Fermi contour is strictly zero. Rather than a simple vanishing photoemission matrix element, the cancellation results from the interference between emission from A and B sites, as shown by Shirley *et al* [37]. This cancellation, like the Dirac nature of the QPs, and the lack of backscattering, follow from the strict A–B atom symmetry. If we break the A–B atom symmetry, we not only open a gap at E_D (thereby destroying the massless character), but also destroy the phase cancellation affecting the Fermi surface intensity.

   These effects are illustrated in figure 6. In figure 6(a), we show as polar maps the measured angular distribution of the band intensity taken about the K point for monolayer and bilayer graphene (closed and open circles, respectively). These data were obtained by fitting the momentum distribution curves (MDCs) taken along radial cuts for an energy window ∼75 meV below E_F. The monolayer and bilayer Fermi surfaces are practically identical, but as indicated in the figure, the bilayer signal is not completely extinguished in any direction. In contrast, for the monolayer, the intensity is completely extinguished in one direction, apart from a very weak minority contribution from bilayer regions. This residual bilayer signal is easy to subtract since it is well separated from the monolayer bands below E_D [14]. After subtraction, we determined that the monolayer band intensity is zero within a very low noise floor (about 0.15% as indicated by the central yellow circle).

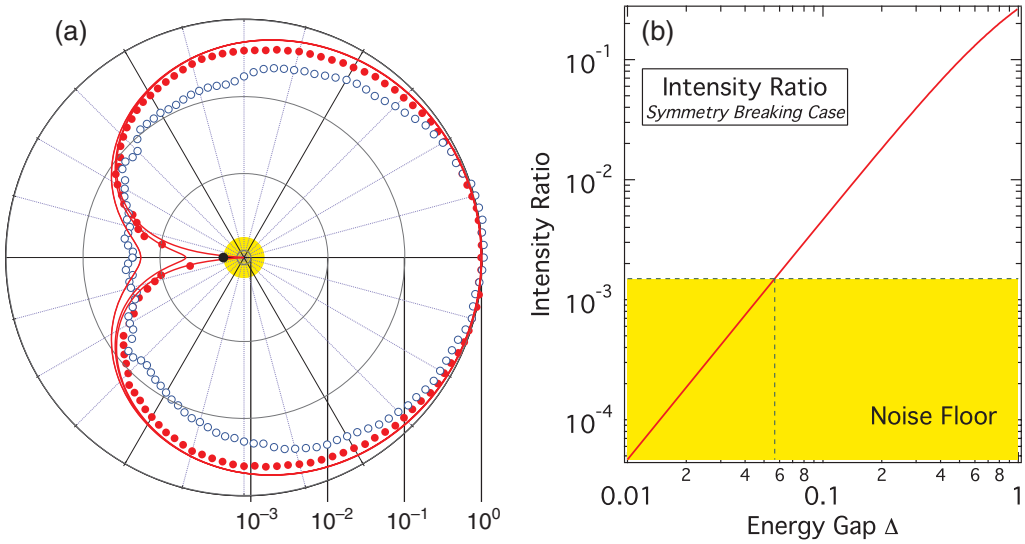

Figure 6. (a) Polar plot of the intensity of the Fermi contours for monolayer (solid circles) and bilayer graphene (open circles), obtained by fitting momentum distribution curves (MDCs) taken along radial cuts through the K point of the Brillouin zone. The intensity scale is logarithmic. Also shown are theoretical intensities for asymmetry parameters $\Delta = 0.0$, 0.1 and 0.2 eV (solid lines) using Shirley's formalism [37]. The solid black data point is an upper limit based on the noise floor indicated by the central yellow circle. (b) The ratio of the weakest to strongest emission intensities as a function of asymmetry parameter Δ. The noise floor (yellow region) establishes the maximum value of the asymmetry parameter ~55 meV admitted by our measured intensity distribution.

Shirley derived a simple formula for the symmetric case $\Delta = 0$ for monolayer graphene; we extended this model to the case of finite Δ and show in figure 6(a) the expected angular distributions for a $\Delta = 0.0, 0.1$ and 0.2 eV (leading to energy gaps at E_D of the same values). This plot shows that we are fairly sensitive to the possible symmetry breaking (and this sensitivity can be enhanced simply by acquiring the bands with better statistics). Figure 6(b) shows a plot of the intensity reduction as a function of Δ, which can be compared to our noise floor (<0.015%). From this comparison, we can conservatively estimate the maximum gap at E_D to be under 60 meV. Since the apparent kink at E_D (with a resulting spreading of the states there) is much wider in energy than this, we can rule out the symmetry breaking as being the dominant factor to explain the anomalous dispersion at E_D.

As an aside, the reason the bilayer is not completely extinguished is that A–B atom symmetry breaking is indeed violated for the bilayer. That is because only one atom (A, say) in the outer layer is directly over an atom in the inner graphene layer (see figure 1). This symmetry breaking also explains the well-known symmetry breaking in STM images of bilayer and thicker films [28, 37]. (A complete model of the bilayer angular intensity profile is outside the scope of this paper and will be presented elsewhere.)

7. It is worth pointing out the very high momentum resolution and accuracy of positioning of the sample that is required to obtain spectra precisely at E_D. In figure 5(a), we see that the entire span of the Fermi bands is only about 0.1 $Å^{-1}$. Only a small misalignment on the order of 0.05° could result in an apparent gap in the bands.

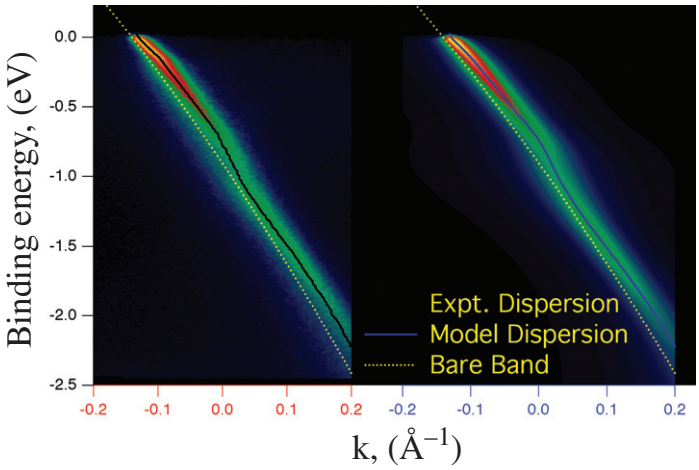

Figure 7. Spectral function of doped graphene. (a) The experimentally determined spectral function for graphene doped with K atoms (total doping $n = 5.6 \times 10^{13}\,\mathrm{cm}^{-2}$). The solid line is the fitted band position $\omega_\mathrm{b}(\mathbf{k}) + \mathrm{Re}\,\Sigma(\mathbf{k}, \omega)$, the dotted line is the bare band $\omega_\mathrm{b}(\mathbf{k})$. (b) A model spectral function generated using only the measured $\mathrm{Im}\,\Sigma(\mathbf{k}, \omega)$ and the bare band $\omega_\mathrm{b}(\mathbf{k})$. Adapted from [15].

3.2. Many-body explanation for anomalies at E_D

3.2.1. The case for self-consistency. Having ruled out the gap scenario, we can now consider many-body interactions to explain the kinked dispersions around E_D. The first issue is whether a self-consistent model is possible even in principle. We will first establish that the kinks and the linewidth variations are consistent with each other. As discussed above and in the literature [18, 38], we analyse the spectral function data in terms of real and imaginary parts of the self-energy function $\Sigma(\mathbf{k}, \omega)$. Figure 7 (b) shows an experimentally acquired spectral function $A(\mathbf{k}, \omega)$ for relatively highly doped graphene ($n = 5.6 \times 10^{13}\,\mathrm{cm}^{-2}$). The dressed band position $\omega = \omega_\mathrm{b}(\mathbf{k}) + \mathrm{Re}\,\Sigma(\mathbf{k}, \omega)$ is determined by fitting MDCs (i.e. individual constant-energy slices) to Lorentzian functions. The positions are plotted in figures 7(a) (black line) and the Lorentzian width as a function of ω is plotted in figure 8(a).

In order to converge to a self-consistent interpretation, it is necessary to iteratively apply the following procedure. We take a second-order polynomial as a trial bare band $\omega_\mathrm{b}(\mathbf{k})$. Given this $\omega_\mathrm{b}(\mathbf{k})$, we can easily scale the MDC widths (units of Å) into the function $\mathrm{Im}\,\Sigma(\mathbf{k}, \omega)$ (units of eV), shown in figure 8(b). This function is smoothed and then Hilbert transformed into a trial $\mathrm{Re}\,\Sigma(\mathbf{k}, \omega)$ function. We can also extract the $\mathrm{Re}\,\Sigma(\mathbf{k}, \omega)$ function by subtracting the trial bare band from the fitted band position. These two $\mathrm{Re}\,\Sigma(\mathbf{k}, \omega)$ functions (figure 7(c)) are compared and the trial bare band adjusted until the models $\mathrm{Re}\,\Sigma(\mathbf{k}, \omega)$ and $\mathrm{Im}\,\Sigma(\mathbf{k}, \omega)$ are in good agreement with the experimentally extracted curves as plotted in figures 7(b) and (c).

As a final check of self-consistency, we can generate a trial spectral function $A(\mathbf{k}, \omega)$ from only the fitted MDC widths and the mathematically transformed $\mathrm{Re}\,\Sigma(\mathbf{k}, \omega)$, shown in figure 7(b). It is in excellent agreement with the experimental function in figure 7(a). Having demonstrated this self-consistency, we can say with high degree of confidence that the kink anomalies must be attributed to many-body interactions, and not any details of the single-particle bandstructure. That is, we can safely rule out not only the superlattice gap scenario outlined above, but also strain, defects and other initial-state effects.

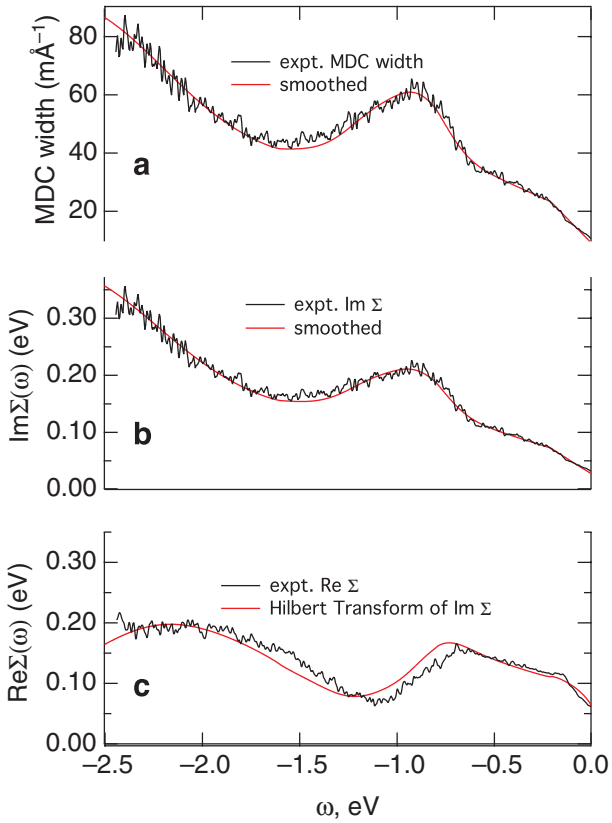

Figure 8. Experimentally determined self-energy function. (a) The width of the MDCs as a function of energy. (b) Im $\Sigma(\mathbf{k}, \omega)$ derived from scaling the MDC widths by half the band velocity (black) and smoothing (red). (c) Re $\Sigma(\mathbf{k}, \omega)$ obtained from the experimental data (black line) and by Hilbert transforming the smoothed Im $\Sigma(\mathbf{k}, \omega)$ (red). The sample is doped to $n = 5.6 \times 10^{13}\,\mathrm{cm}^{-2}$.

3.2.2. Contributions to scattering lifetime. We now explain the physical origin of the measured Im $\Sigma(\mathbf{k}, \omega)$ function in more quantitative fashion. For convenience, we work with the fitted MDC widths, which are plotted in figure 9(a). The features to explain are, starting from zero energy, the monotonic increase in lifetime down to about -0.2 eV; the hump at around $E_D = -1.0$ eV, and the remaining background rise. These were attributed [15] to e–ph coupling, e–pl coupling, and e–h pair generation; computations of these contributions to the scattering rate are shown in figure 9(b). Schematic diagrams of these processes are shown in figure 10.

We can meaningfully consider only those excitations whose energy scale is greater than our energy resolution ($\sim$25 meV). Considering the energy scale of the observed kink anomalies ($\geqslant$200 meV) we can rule out any significant interactions between 25 and 200 meV, such as scattering from low-energy acoustical vibrational modes.

First, we qualitatively discuss the coupling to phonons at the 200 meV energy scale (a quantitative analysis has been presented by Bostwick *et al* [13] for graphene, and for other surfaces in [40]–[42]). Since this energy is much larger than our temperature ($k_B T \sim 2$ meV, we can rule out phonon absorption and consider only decay of QPs by phonon emission (figure 10(a)). Such QP decays are forbidden for states at E_F, but become available as the QP energy increases.

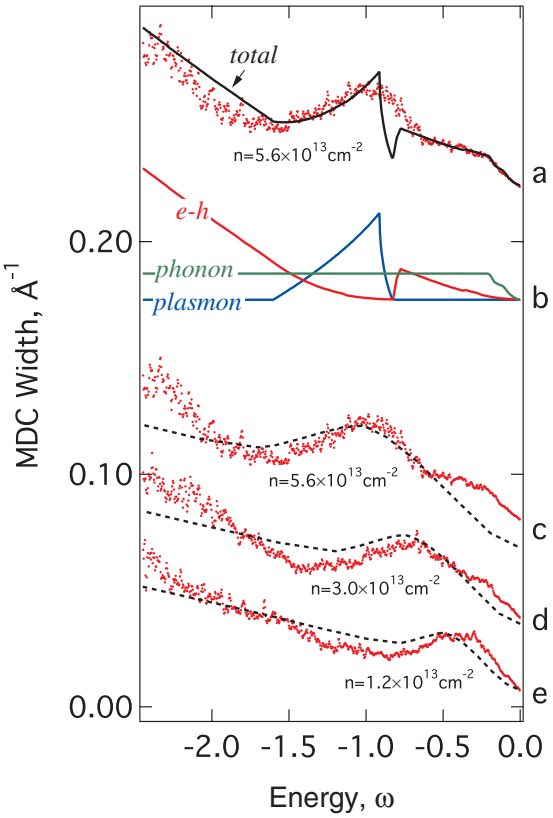

Figure 9. Comparison of calculated and measured MDC widths. (a) Measured MDC widths (dots) for the highest-doping sample ($n = 5.6 \times 10^{13}$ cm^{-2}) are compared to the total scattering rate contribution from Bostwick *et al* [15] (solid). (b) The calculated contributions to the scattering rate due to electron–hole (e–h) pair generation, e–ph scattering, and e–pl scattering [15]. (c)–(e) Experimental MDC widths for $n = 1.2$, 3.0 and $n = 5.6 \times 10^{13}$cm^{-2} in comparison to the calculations of Hwang *et al* [39]. Adapted from [15].

Typically once the QP energy is greater than the phonon energy scale, the lifetime due to scattering is independent of QP energy. This change in QP lifetime is reflected in a monotonic increase in the imaginary part of the self energy Im $\Sigma(\mathbf{k}, \omega)$. Because the real and imaginary parts of $\Sigma(\mathbf{k}, \omega)$ are related by Hilbert transform, one expects to see a non-trivial change in the dispersion on the phonon energy scale, which is observed as a kink. Physically, we interpret the change of band slope between the kink and E_F as a renormalization of the mass as the QPs become 'dressed' with a virtual cloud of phonons. But we know that the QPs in graphene are effectively massless, so we speak in terms of a velocity renormalization (or equivalently a renormalization of the relativistic mass-equivalent energy).

The 200 meV kink is stronger for the K-covered graphene compared to the as-grown surface (see figure 3(a) and (b)) due to a phase-space argument. The density of electronic states in **k**-space is a constant, so that as the sample is doped, the bands span more electronic states near E_F; as these become available final states for phonon scattering, the decay probability increases. Left unexplained is the overall magnitude of the e–ph scattering rate at all dopings, which is about six times stronger than what is predicted by the normal deformation potential calculations [13, 43, 44].

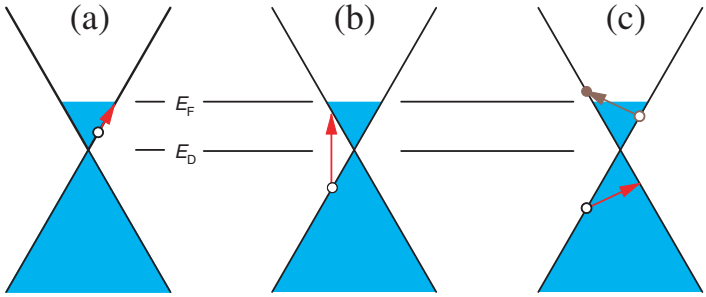

Figure 10. Possible many-body decay process in n-doped graphene. (a) decay by e–ph emission (b) decay by e–pl emission (c) decay by e–h pair generation.

The quantitative analysis of the phonon kink [13, 15], which followed the standard formalism [45], is quite useful but does not perfectly describe the kink strength (it underestimates it slightly) and furthermore does not take into account the actual band structure of graphene: the actual phonon scattering rate should diminish near E_D from the same phase-space argument just cited. A first-principle calculation of the phonon scattering rate should account for both of these effects.

In the case of the second kink near E_D, the QP decay is through emission of plasmons (figure 10(b)), which is favoured over phonon scattering because of the kinematic constraints [15, 39, 46]. Whereas optical phonons are more or less delocalized in **k**-space with fixed energy scale, the plasmon spectrum in graphene has a fast energy dispersion in a narrow range of **k**. This follows from the dispersion relation for 2D plasmons [47] in the long wavelength limit:

$$\omega_{\mathrm{pl}}(q) = \sqrt{4\pi n e^2 q/m(1+\epsilon)}, \tag{3}$$

where q is the plasmon momentum, m is the carrier mass, and $\epsilon \sim 6$ is the dielectric constant [13]. Although plasmons in principle exist in the domain $0 < q < \infty$, in practice they propagate freely up to a critical momentum $q < q_c$ due to Landau damping (plasmon decay into e–h- pairs) [48].

For graphene, the rest mass m is zero near E_D, but the relativistic mass equivalent to the kinetic energy, $m_r = E/v^2$ (where v is the Fermi velocity), is on the order [2, 3] of $0.1\,m_e$ and can be used to set the plasmon energy scale ω_{pl}. This means that more or less vertical interband decays by plasmon scattering are now the dominant factor determining the lifetime near E_D.

Two other contributions to the scattering lifetime must be considered. First is defect or impurity scattering. Normally, the defect scattering is taken to be a constant background to the imaginary self energy Im $\Sigma(\mathbf{k}, \omega)$, which is a deconvolution of the residual momentum spread of the bands at E_F and the instrumental function. In our case, the residual momentum spread is only about $0.005\,\text{Å}^{-1}$, which is comparable to our instrumental resolution, so we can safely discard the defect scattering rate as negligible.

The remaining contribution to the scattering rate is the decay by e–h pair generation, which is the standard decay process in Fermi liquid theory. In this process (figure 10(c)), the decay of the QP is accompanied by an excitation of an electron above E_F, creating a new hole below E_F. For 2D metals with circular Fermi surface, Hodges *et al* [49] proved the famous rule that e–h-pair scattering rate goes as $\omega^2 \ln \omega$. This was determined by a phase space integration of all possible kinematically allowed e–h-scattering processes. For a 2D free electron gas this could be carried out analytically, but for graphene, we evaluated the appropriate integral numerically.

This was done so that we could use the experimentally determined dispersion (although we assumed cylindrical symmetry and zero temperature to simplify the integration).

The most interesting finding is that for n-doped graphene, the e–h-scattering rate rises from E_F down towards E_D as it would be expected for any metal. Around E_D, however, the scattering rate must necessarily drop, because in the vicinity of E_D, the decays are mostly vertical transitions. Such a decay by e–h-pair generation is forbidden since we cannot find a momentum-conserving excitation near E_F to satisfy the kinematic constraints. Only at energy scale around twice the Dirac energy do such excitations become available, and we see an associated rise in the scattering rate at high-energy scales.

Considering the simplicity of the model, the total scattering rate function (figure 9(b)) does a remarkably good job of modelling the data. Theoretical modelling of the e–pl and e–h scattering rates has also been performed by Hwang *et al* [39]. Figures 9(c) and (e) shows a comparison of our measured MDC widths to their model for three different dopings. Although they overestimate the relative contribution of the e–pl to e–h processes, their calculation is in excellent qualitative agreement with the observed MDC widths. The main discrepancy is the failure of the model to account for the scattering rate from phonons, which was not included in their calculation.

The many-body effects we measure are present all the way down to zero doping and therefore may play a role in the transport of gated graphene devices. These are much more dilute carrier gases than we achieved by alkali metal doping. As the doping level decreases, the phonon and plasmon processes will overlap in energy and therefore will not be separable. This is already seen in the lowest doping we probed (figure 9(c)). The plasmon and e–h pair scattering rates are reasonably separable at all dopings, but there is an energy overlap region just above E_D where neither alone is a good description of the total electron–electron interaction. These observations imply that a proper description of the scattering rate will take into account much more complicated processes than in our simple treatment. In the language of Feynman diagrams, it means higher-order diagrams that are typically considered will be necessary to model the photoemission data. In addition, when E_F is reduced to be comparable to the temperature, thermal excitation effects will increase in importance. This has already been discussed in relation to plasmons [46].

3.3. Out-of-plane symmetry breaking in multilayer graphene

Multilayer graphene films grown on silicon carbide have an obvious built-in symmetry breaking, because of the inequivalence of the two film interfaces (SiC and vacuum). Further symmetry breaking can be induced by either external field, or by growth of additional layers on top of the graphene films. Understanding these symmetry effects is important in order to exploit them for technological purposes. Extension of the Hamiltonian in equation (2) to multiple layers gives a simple framework to achieve this.

Extension to two layers is achieved by adding an additional hopping term between the B atoms of the first layer and the A atoms of the second layer [25, 30, 50, 51]:

$$\mathcal{H} = \begin{pmatrix} E_1 & v\pi^\dagger & 0 & 0 \\ v\pi & E_1 & \gamma_1 & 0 \\ 0 & \gamma_1 & E_2 & v\pi^\dagger \\ 0 & 0 & v\pi & E_2 \end{pmatrix} \equiv \begin{pmatrix} \alpha_1 & \beta_0 \\ \beta_0^T & \alpha 2 \end{pmatrix}. \tag{4}$$

Here α_i acts with respect to the (A, B) sublattices of the ith layer, and β_0 is a 2×2 matrix

$$\beta_0 \equiv \mathcal{H} = \begin{pmatrix} 0 & 0 \\ \gamma_1 & 0 \end{pmatrix}, \tag{5}$$

where γ_1 is the hopping parameter between layers. The wavefunction now has four elements with basis set orbitals located at A_1, B_1, A_2 and B_2 atoms, where i is the layer number (1 or 2).

There are two further generalizations of equation (4), firstly, by adding more layers, and secondly, by altering the stacking sequence [52]. Adding a third layer, one couples the B atom of the second layer to the A atom of the third for conventional Bernal-type stacking (ABAB . . .) characteristic of bulk graphite. Repeating this sequence we come to the Bernal Hamiltonian for N layers,

$$\mathcal{H} = \begin{pmatrix} \alpha_1 & \beta_0 & & & & \\ \beta_0^{\mathrm{T}} & \alpha_2 & \beta_0^{\mathrm{T}} & & & \\ & \beta_0 & \alpha_3 & \beta_0 & & \\ & & \beta_0^{\mathrm{T}} & \alpha_4 & \beta_0^{\mathrm{T}} & \\ & & & \beta_0 & \ddots & \\ & & & & & \alpha_{\mathrm{N}} \end{pmatrix}, \quad \text{(Bernal)}. \tag{6}$$

A useful generalization of equation (6) is

$$\mathcal{H} = \begin{pmatrix} \alpha_1 & \beta_0 & & & & \\ \beta_0^{\mathrm{T}} & \alpha_2 & \beta_s & & & \\ & \beta_s^{\mathrm{T}} & \alpha_3 & \beta_0 & & \\ & & \beta_0^{\mathrm{T}} & \alpha_4 & \beta_s & \\ & & & \beta_s^{\mathrm{T}} & \ddots & \\ & & & & & \alpha_{\mathrm{N}} \end{pmatrix}, \quad \text{(general)}, \tag{7}$$

where

$$\beta_s = \gamma_1 \begin{pmatrix} 0 & s \\ 1-s & 0 \end{pmatrix}. \tag{8}$$

Now, if $s = 0$, then equation (7) is the Hamiltonian for Bernal stacking, while for $s = 1$, equation (7) is the Hamiltonian for rhombohedral stacking (ABCABC . . .). We can further generalize this Hamiltonian to arbitrary stacking orders, by suitably choosing the different values of s in each block of the matrix.

In the above Hamiltonians, we have assigned to each layer its own on-site Coulomb energy E_i. This allows for the possibility of a poorly screened electric field across the FLG film, which is reasonable in view of the predicted long screening lengths in this direction. It is straightforward to show that the Dirac crossing energy is $E_{\mathrm{D}} = \mathrm{Tr}\mathcal{H}/2N$ where N is the number of layers.

Figure 11 shows the calculated bandstructures for 1–4 layers graphene. The calculations were for either Bernal (solid lines) or rhombohedral (dashed lines); the distinction is obviously

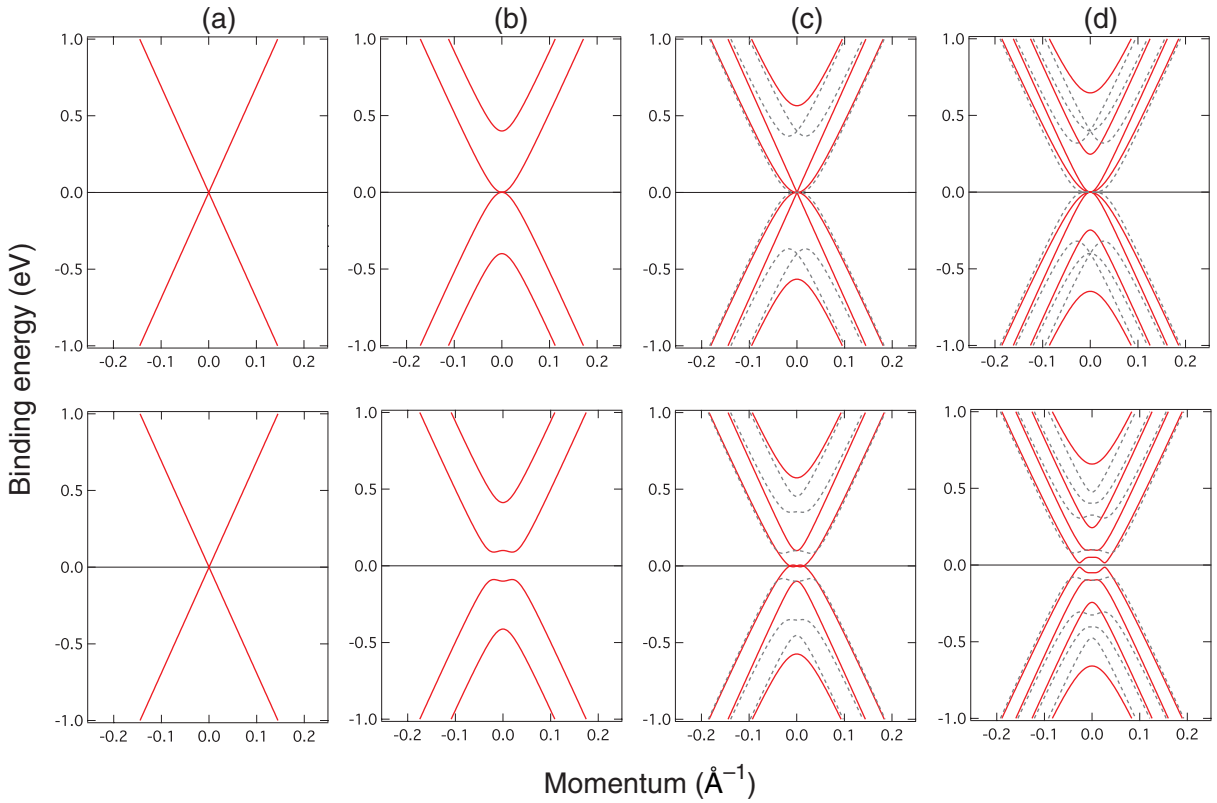

Figure 11. Calculated band structures for FLG using equation (7). (a)–(d) show the bands for 1–4 layers graphene, respectively. The upper panels are for unbiased layers ($E_i = 0$) while the lower panels were calculated with a 200 meV potential difference across the films, assuming a linear field gradient. Calculations were for $\gamma_1 = 0.4$ eV and $v = 6.91$ eV Å^{-1}.

meaningful only for films with $N \geqslant 3$ layers. Far from E_D, it turns out that there is little distinction between rhombohedral and Bernal stacking. This is to our advantage, because as figure 11 shows, one can know the film thickness directly from band structure measurements by simply counting the number of π bands below E_D. Near E_D, the situation is quite different, since the two stacking types have quite different band dispersions. (Similar calculations have also been carried out with *ab initio* models [26, 27], [53]–[55].)

The detailed bandstructure around E_D shows a strong sensitivity to the Coulomb energy terms E_i that enter the Hamiltonian matrix (equations (2) and (7)) [30]. This can be seen by comparing the upper and lower rows of figure 11 which were calculated for two cases. In the first case, the energies E_i are all zero, and we find a gapless energy spectrum at $E_F = E_D$. For the lower row, we distributed a field change $U = 200$ meV across the film in uniform increments, which simulates FLG in a bias or inhomogeneously-doped geometry. This procedure opens gaps near E_D; for the special bilayer case $N = 2$, there is a complete gap at the Fermi level. This gap was proposed to be the basis of a new kind of electronic switch, whereby lateral transport through the bilayer could be modulated by applying a modest field perpendicular to the film [14, 56, 57].

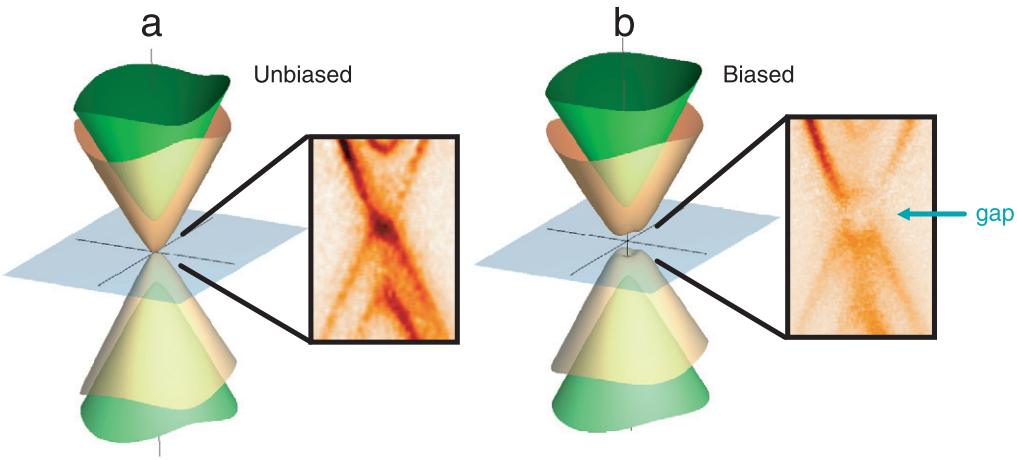

Figure 12. Gap control of bilayer graphene. (a) An unbiased bilayer has a gapless spectrum, which we could observe for a doped sample which carefully balanced the field across the film. (b) For a bilayer with a field gradient, an energy gap is opened between π and π^* states.

Systematic studies of the thickness and doping dependence by ARPES have been presented by Ohta *et al* [14, 25]. Figure 12 shows the bilayer graphene bandstructure in two different field geometries, achieved by doping a bilayer graphene on SiC [14]. Similar to monolayer graphene, the as-grown bilayer films have an intrinsic n-doping, which allows us to probe the states both above and below E_D. Because the doped carriers are concentrated in the interface layer, the as-grown films have a field gradient across them and hence a gap at E_D. Carefully balancing this charge imbalance allows us to close the gap (figure 12(a)), while further doping of the surface layer allows us to create a net charge imbalance, thus reopening the gap (figure 12(b)). Evidence for a similar gap opening was also presented for the surface layers of graphite when doped with Na [58].

Systematic thickness measurements at constant doping were presented by Ohta *et al* [25]. For films of thickness $N = 1$–4 layers, we found that the total charge density donated from the substrate was the same for all thicknesses. Similar to bilayer graphene, the charge was donated predominantly to the interface graphene layer. This is in accord with the metallic nature of the films, which can screen the interface layer from the rest of the film. The measured bandstructures for $N = 1$–4 layers are shown in figure 13.

These spectra are very rich in information: we could determine not only the number of layers (by counting the number of π states below E_D straightforwardly) but also derive the stacking order. One can see easily for $N = 3$ that there are two states (marked by circles) of equal intensity that can only be ascribed to equal populations of Bernal and rhombohedral stacking. For quadlayer (and presumably thicker) careful analysis shows that Bernal stacking predominates. This can be taken as evidence for the role of second near-neighbour interactions to stabilize the Bernal stacking type in graphite.

The electronic information that could be derived from the data are equally rich: in analogy with the bilayer analysis, we could assign the different charge densities in each graphene layer,

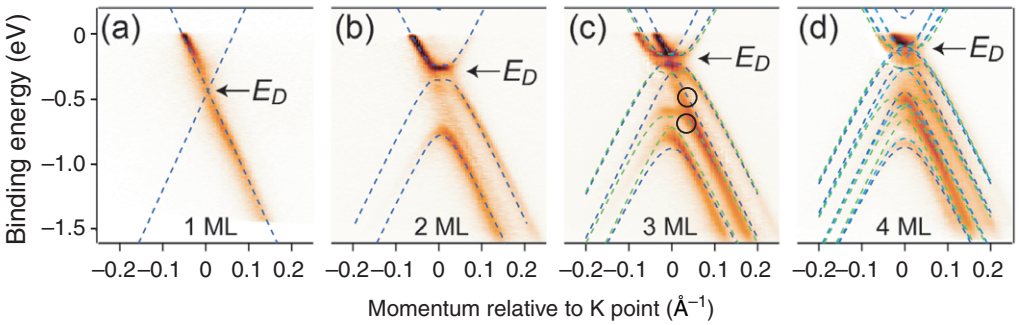

Figure 13. Band structure of graphene films of thickness for (a)–(d) $N = 1$–4 layers, respectively. Calculated bands for three configurations are shown: Bernal stackings ABAB and ABAC (blue and light blue, respectively) and rhombohedral stackings (red). Adapted from [25].

and determine the out-of-plane screening length. In the formation of the graphene films, about 1×10^{13} carriers cm^{-2} are donated to the film, with, in general about 85% of the charge donated to the first layer, and most of the rest in the second layer [25].

3.4. Conclusions and outlook: graphene, the simplest complex material

In the last few years, there was an explosion of interest in graphene since isolation of high-quality samples was achieved and since its many novel properties were elucidated both experimentally and theoretically. Seldom does a new material come along that has such strong fundamental and practical interest. From an experimental point of view, graphene is highly attractive since unlike other low-dimensional materials (such as high-mobility semiconductor 2D electron gases), graphene films are exposed to vacuum and can be directly probed by surface-sensitive techniques such as LEED, STM and ARPES. ARPES has a special role to play because it is sensitive not only to the valence band energy structure but also its symmetry in **k**-space. Furthermore it can give direct information on the many-body interactions, such as mass renormalization. Through graphene's special sensitivity to symmetry, we could even derive much structural information such as stacking errors and electronic information such as charge density and screening length, which would be very hard to achieve with other probes.

In our opinion, graphene is unique in many ways. It is the first system to our knowledge to show e–pl coupling in the ARPES signal, which suggests not only the exciting possibility of new coupling mechanisms, but also technological implications in the interaction with photons. Finally, it is a model system for correlation and many-body interactions which can supply stringent tests for theory.

References

[1] Novoselov K S, Geim A K, Morosov S V, Jiang D, Zhang Y, Dubonos S V, Grigorieva I V and Firsov A A 2004 Electric field effect in atomically thin carbon films *Science* **306** 666

[2] Novoselov K S, McCann E, Morosov S V, Fal'ko V I, Katsnelson M I, Zeitler U, Jiang D, Schedin F and Geim A K 2005 Two-dimensional gas of massless Dirac fermions in graphene *Nature* **438** 192–200

[3] Zhang Y, Tan Y W, Stormer H L and Kim P 2005 Experimental observation of the quantum Hall effect and Berry's phase in graphene *Nature* **438** 201–4
[4] Berger C *et al* 2006 Electronic confinement and coherence in patterned epitaxial graphene *Science* **312** 1191–6
[5] Katsnelson M I and Novoselov K S 2007 Graphene: new bridge between condensed matter physics and quantum electrodynamics *Preprint* cond-mat/0703374
[6] Ando T and Nakanishi T 1998 Impurity scattering in carbon nanotubes—absence of back scattering *J. Phys. Soc. Japan* **67** 1704–13
[7] Ando T, Nakanishi T and Saito R 1998 Berry's phase and absence of back scattering in carbon nanotubes *J. Phys. Soc. Japan* **67** 2857–62
[8] Forbeaux I, Themlin J M and Debever J M 1998 Heteroepitaxial graphite on 6H-SiC(0001): interface formation through conduction-band electronic structure *Phys. Rev.* B **58** 16396–406
[9] Berger C *et al* 2004 Ultrathin epitaxial graphite: 2d electron gas properties and a route toward graphene-based nanoelectronics *J. Phys. Chem.* B **108** 19912–6
[10] Jones H 1934 Applications of the Bloch theory to the study of alloys and of the properties of bismuth *Proc. R. Soc. Lond.* A **147** 396–417
[11] Reich S, Maultzsch J, Thomsen C and Ordejn P 2002 Tight-binding description of graphene *Phys. Rev.* B **66** 035412
[12] Saito R, Dresselhaus G and Dresselhaus M S 1998 *Physical Properties of Carbon Nanotubes* (London: Imperial College Press)
[13] Bostwick A, Ohta T, McChesney J L, Seyller T, Horn K and Rotenberg E 2007 Renormalization of graphene bands by many-body interactions *Solid State Commun.* **143** 63–71
[14] Ohta T, Bostwick B, Seyller T, Horn K and Rotenberg E 2006 Controlling the electronic structure of bilayer graphene *Science* **313** 951–4
[15] Bostwick A, Ohta T, Seyller T, Horn K and Rotenberg E 2007 Quasiparticle dynamics in graphene *Nat. Phys.* **3** 36–40
[16] Wehling T O, Novoselov K S, Morosov S V, Vdovin E E, Katsnelson M I, Geim A K and Lichtenstein A I 2007 Molecular doping of graphene *Preprint* cond-mat/0703390
[17] Damascelli A, Hussain Z and Shen Z X 2003 Angle-resolved photoemission studies of the cuprate super conductors *Rev. Mod. Phys.* **75** 473
[18] Kaminski A and Fretwell H M 2005 On the extraction of the self-energy from angle-resolved photoemission spectroscopy *New J. Phys.* **7** 98
[19] Strocov V N, Charrier A, Themlin J M, Rohlfing M, Claessen R, Barrett N, Avila J, Sanchez J and Asensio M C 2001 Photoemission from graphite: intrinsic and self-energy effects *Phys. Rev.* B **64** 075105
[20] Kihlgren T, Balasubramanian T, Walldén L and Yakimova R 2002 Narrow photoemission lines from graphite valence states *Phys. Rev.* B **66** 235422
[21] Soe W H, Rieder K H, Shikin A M, Mozhaiskii V, Varykhalov A and Rader O 2004 Surface phonon and valence band dispersions in graphite overlayers formed by solid-state graphitization of 6H-SiC(0001) *Phys. Rev.* B **70** 115421
[22] Rollings E, Gweon G H, Zhou S Y, Mun B S, McChesney J L, Hussain B S, Fedorov A V, First P N, de Heer W A and Lanzara A 2006 Synthesis and characterization of atomically thin graphite films on a silicon carbide substrate *J. Phys. Chem. Solids* **67** 2172–7
[23] Seyller Th, Emtsev K V, Speck F, Gao K Y and Ley L 2006 Schottky barrier between 6H-SiC and graphite: implications for metal/SiC contact formation *Appl. Phys. Lett.* **88** 242103
[24] Emtsev K V, Seyller Th, Speck F, Ley L, Stojanov P, Riley J D and Leckey R G C 2006 Initial stages of the graphite-SiC(0001) interface formation studied by photoelectron spectroscopy *Preprint* cond-mat/0609383
[25] Ohta T, Bostwick A, McChesney J L, Seyller T, Horn K and Rotenberg E 2007 Interlayer interaction and electronic screening in multilayer graphene investigated with angle-resolved photoemission spectroscopy *Phys. Rev. Lett.* **98** 206802–4

[26] Varchon F *et al* 2007 Electronic structure of epitaxial graphene layers on SiC: effect of the substrate *Preprint* cond-mat/0702311
[27] Mattausch A and Pankratov O 2007 *Ab initio* study of graphene on SiC *Preprint* cond-mat/07040216
[28] Mallet P, Varchon F, Naud C, Magaud L, Berger C and Veuillen J-Y 2007 Electron states of mono- and bilayer graphene on SiC probed by STM *Preprint* cond-mat/0702406
[29] DiVincenzo D P and Mele E J 1984 Self-consistent effective-mass theory for intralayer screening in graphite intercalation compounds *Phys. Rev.* B **29** 1685
[30] McCann E and Fal'ko V I 2006 Landau-level degeneracy and quantum Hall effect in a graphite bilayer *Phys. Rev. Lett.* **96** 086805
[31] Zhou S Y, Gweon G H and Lanzara A 2006 Low energy excitations in graphite: the role of dimensionality and lattice defects *Ann. Phys.* **321** 1730–46
[32] Sugawara K, Sato T, Souma S, Takahashi T and Suematsu H 2007 Anomalous quasiparticle lifetime and strong electron-phonon coupling in graphite *Phys. Rev. Lett.* **98** 036801
[33] Lanzara A 2007 First Direct observation of Dirac fermions in graphite *Bull. Am. Phys. Soc.* **52** A3.00004
[34] Zhou S Y, Gweon G H, Graf J, Siegel D, Rollings E and Lanzara A 2007 ARPES study of the electronic dynamics from graphene to graphite *Bull. Am. Phys. Soc.* **52** L8.00008
[35] Rotenberg E, Koh H, Rossnagel K, Yeom H W, Schäfer J, Krenzer B, Rocha M P and Kevan S D 2003 $\sqrt{7} \times \sqrt{3}$ on Si(111): a nearly free electron metal in two dimensions *Phys. Rev. Lett.* **91** 246404
[36] Crain J N, Altmann K N, Bromberger C and Himpsel F J 2002 Fermi surfaces of surface states on Si(111)-Ag, Au *Phys. Rev.* B **66** 205302
[37] Shirley E L, Terminello L J, Santoni A and Himpsel F J 1995 Brillouin-zone-selection effects in graphite photoelectron angular distributions *Phys. Rev.* B **51** 13614–22
[38] Kordyuk A A, Borisenko S V, Koitzsch A, Fink J, Knupfer M and Berger H 2005 Bare electron dispersion from experiment: self-consistent self-energy analysis of photoemission data *Phys. Rev.* B **71** 214513
[39] Hwang E H, Yu-Kuang Hu B and Das Sarma S 2006 Inelastic carrier lifetime in graphene *Preprint* cond-mat/0612345
[40] Valla T, Fedorov A V, Johnson P D and Hulbert S L 1999 Many-body effects in angle-resolved photoemission: quasiparticle energy and lifetime of a Mo(110) suface state *Phys. Rev. Lett.* **83** 2085–8
[41] Hengsberger M, Purdie D, Segovia P, Garnier M and Baer Y 1999 Photoemission study of a strongly coupled electron–phonon system *Phys. Rev. Lett.* **83** 592–5
[42] Rotenberg E, Schaefer J and Kevan S D 2000 Coupling between adsorbate vibrations and an electronic surface state *Phys. Rev. Lett.* **84** 2925–8
[43] Calandra M and Mauri F 2005 Theoretical explanation of superconductivity in C_6Ca *Phys. Rev. Lett.* **95** 237002
[44] Calandra M and Mauri F 2006 Origin of superconductivity of CaC_6 and of other intercalated graphites *Phys. Status Solidi* b **243** 3458–63
[45] Grimvall G 1981 *The Electron Phonon Interaction in Metals* (Amsterdam: North Holland)
[46] Vafek O 2006 Thermoplasma polariton within scaling theory of single-layer graphene *Phys. Rev. Lett.* **97** 266406
[47] Stern F 1967 Polarizability of a two-dimensional electron gas *Phys. Rev. Lett.* **18** 546
[48] Kliewer K L and Raether H 1973 Plasmon observation using x-rays *Phys. Rev. Lett.* **30** 971
[49] Hodges C, Smith H and Wilkins J W 1971 Effect of Fermi surface geometry on electron-electron scattering *Phys. Rev.* B **4** 302
[50] McCann E 2006 Asymmetry gap in the electronic band structure of bilayer graphene *Preprint* cond-mat/0608221
[51] Novoselov K S, Geim A K, Morosov S V, Fal'ko V I, Katsnelson M I, Zeitler U, Jiang D, Schedin F and Geim A K 2006 Unconventional quantum Hall effect and Berry's phase of 2 in bilayer graphene *Nat. Phys.* **2** 177–80
[52] Guinea F, Castro Neto A H and Peres N M R 2006 Electronic states and Landau levels in graphene stacks *Preprint* cond-mat/0604396

[53] Min H, Sahu B, Banerjee S K and MacDonald A H 2007 *Ab initio* theory of gate induced gaps in graphene bilayers *Phys. Rev.* B **75** 155115–7

[54] Wang Z F, Li Q, Su H, Wang X, Shi Q W, Chen J, Yang J and Hou J G 2007 Electronic structure of bilayer graphene: a real-space green's function study *Phys. Rev.* B **75** 085424

[55] Aoki M and Amawashi H 2007 Dependence of band structures on stacking and field in layered graphene *Preprint* cond-mat/0702257

[56] Nilsson J, Castro Neto A H, Guinea F and Peres N M R 2006 Transmission through a biased graphene bilayer barrier *Preprint* cond-mat/0607343

[57] Castro E V, Novoselov K S, Morosov S V, Peres N M R, Lopes dos Santos J M P, Nilsson J, Guinea F, Geim A K and Castro Neto A H 2006 Biased bilayer graphene: semiconductor with a gap tunable by electric field effect *Preprint* cond-mat/0611342

[58] Pivetta M, Patthey F, Barke I, Hovel H, Delley B and Schneider W-D 2005 Gap opening in the surface electronic structure of graphite induced by adsorption of alkali atoms: photoemission experiments and density functional calculations *Phys. Rev.* B **71** 165430